Machine Learning Enables Inverse Design of Optically Driven Microscopic Metavehicles

Citation for the original published paper (version of record):
Mylnikov, V., Shanei, M., Käll, M. (2026). Machine Learning Enables Inverse Design of Optically Driven Microscopic Metavehicles. Advanced Optical Materials, 14(26).
http://dx.doi.org/10.1002/adom.71396

Advanced Optical Materials

ADVANCED OPTICAL MATERIALS
www.advopticalmat.de

RESEARCH ARTICLE OPEN ACCESS

Machine Learning Enables Inverse Design of Optically Driven Microscopic Metavehicles

Vasilii Mylnikov | Mahdi Shanei | Mikael Käll

Department of Physics and Astronomy, Chalmers University of Technology, Gothenburg, Sweden

Correspondence: Mikael Käll (mikael.kall@chalmers.se)

Received: 27 January 2026 | **Revised:** 18 May 2026 | **Accepted:** 3 June 2026

Keywords: inverse design | machine learning | metasurface | metavehicle | optical force

ABSTRACT

Lateral optical forces can propel microscopic objects across a surface even when the incident light carries no net momentum in the propagation direction. Here we explore how machine-learning-based inverse design can optimize this process for metavehicles— flat microparticles incorporating silicon metagratings that deflect light at high angles. The optimized design achieves a maximum unidirectional normal-to-lateral momentum deflection efficiency of ~88%, representing a 6% improvement over the best fabricable training-set structure and ~60% improvement compared to the original metavehicle structure. Optimized metavehicles exhibit lateral propulsion speeds in water significantly higher than previously reported. The results demonstrate that inverse design guided by machine learning can substantially enhance optomechanical performance, paving the way toward efficient light-driven micro-transporters and actuators for microbiology and microfluidics. In addition, our strategy yields a library of high-efficiency metagrating designs for diverse photonic components, including high-numerical-aperture axicons, metalenses, and beam deflectors.

1 | Introduction

Optical metasurfaces, typically in the form of dense 2D layers of carefully crafted subwavelength scatterers, can be designed to reshape the wavefront and polarization state of an impinging light field almost at will [1–4]. This process is associated with a change in the linear and angular momentum content of the light-field and a concomitant momentum transfer to the metasurface itself, since total momentum needs to be conserved in the light-matter interaction. The resulting optical recoil forces and torques acting back on the metasurface are typically too weak to be relevant in photonics. However, in certain cases they become critical and form the basis for applications. For example, it has recently been shown that a metasurface suspended in a cavity standing wave can be designed to exhibit both attractive and repulsive radiation pressure forces [5]. Furthermore, research on light sails indicates that optically levitated metasurfaces can be designed to self-stabilize within a laser beam [6–10], which is crucial for reaching the high speeds required for deep-space exploration. A third example, and the focus of this study, is "metavehicles" – microscopic metastructures capable of navigating across a surface in water under unstructured plane-wave illumination while being steered via the incident polarization [11]. Metavehicles are designed to convert the radiation pressure force from a normally incident laser beam into a lateral propulsion force via beam-bending [12], and they take full advantage of the low mass and drag enabled by flat metaoptics [11, 13]. By combining several such beam-bending metasurfaces in a single microstructure, it is possible to construct "metaspinners" [14] and "metarotors" [15] that generate orbital angular momentum and torque from unstructured incident light. It is even possible to transform metavehicles into tiny cogwheels and geared mechanisms for optically driven micromachinery [16].

The main application potential of metavehicles and related optically driven flat microstructures [17, 18] likely lies in microfluidics and contact-free manipulation of biological particles. For example, metavehicles have been shown to act as transporters of microscopic cargo, including yeast cells, and metarotors can be used rotate hundreds of passive microparticles in solution [11, 15]. In such applications, it is crucial to keep the incident light intensity low to avoid harmful photothermal heating, which implies that the normal-to-lateral momentum conversion efficiency should be optimized to be as close to 100% as possible. Fortunately, a wide range of metasurface optimization methodologies has been developed [19]. These include well-established gradient descent [20] and particle swarm optimization [21, 22] methods, which can be successfully applied to metasurfaces with few degrees of freedom (DOF), as well as more sophisticated algorithms [23], such as "objective-first" methods [24], topology optimization [25–28], hybrid methods [29], and inverse design via machine learning [30, 31].

Here, we employ machine-learning-based inverse design to optimize lateral force generation in a metavehicle system, achieving record-high momentum deflection efficiencies and significantly increased propagation speeds in water. The force-generating metastructure has six geometrical DOF, which could, in principle, be optimized using traditional methods. However, by implementing a machine-learning-based inverse-design algorithm, we are able to rapidly generate a large number of highly efficient structures with varying geometrical parameters, which is advantageous when fabrication constraints are taken into account. Our work establishes an efficient and general framework for the inverse design of optically driven micromachines of various kinds, with potential applications in microfluidics, microbiology, and the broader field of metaoptics.

2 | Results and Discussion

2.1 | Optical Functionality, Metagrating Structure, and Fitness Function

The metasurface structure we study is similar to that reported on in [14, 15]: a 1D Si metagrating embedded in SiO_2 that functions as a unidirectional high-angle deflector for normally incident and linearly polarized 1064 nm laser light (Figure 1A). Conservation of linear momentum in the light-metagrating system implies that a lateral reaction force, which can propel the metavehicle across an interface, is induced as a consequence of asymmetric diffraction. The force is maximized for polarization within the metagrating plane of diffraction, in which case it can be approximated as:

$$F = -\frac{n}{2c_0} P_0 \sum_i (T_i + R_i) \sin(\theta_i) \tag{1}$$

where n is the refractive index of the embedding medium, c_0 is the speed of light, and P_0 is the optical power incident on the metagrating. The efficiency of lateral force generation is determined by the power transmission (T_i) and reflection (R_i) diffraction efficiencies and their corresponding diffraction angles θ_i (Figure 1A), where i signifies a diffraction order (here $i = +1$, 0, or -1).

Based on previous works [14, 15], we focus on metagratings with unit cells that contain three Si ridges of varying widths $W_1 < W_2 < W_3$, such that each unit cell acts as a unidirectional optical antenna. All ridges have the same height H and edge-to-edge gap distance g (Figure S1A). Fabrication constraints limit the smallest dimensions to $g > 70$ nm and $W_1 \geq 60$ nm. The periodicity P determines the first-order diffraction angle $\theta_{\pm1}$. Since the Si metagrating is embedded in SiO_2 ($n = 1.45$, total thickness 1 µm), we need to take refraction at the SiO_2 – water ($n = 1.33$) interface into account using the Snell and Fresnel formulas, but we neglect multiple reflections within the metavehicle structure. We consider diffraction angles $\theta_{\pm1} = 50°$ – 65° in SiO_2, which remains below the 66.5° critical angle of the SiO_2–water interface. Based on Equation (1), we now want to optimize the six DOF (P, H, W_1, W_2, W_3, g) to maximize the fitness function:

$$f = (T_{+1w} + R_{+1w} - T_{-1w} - R_{-1w}) \cdot \sin(|\theta_w|) \tag{2}$$

where $|\theta_w| = \arcsin(\lambda_0/1.33P)$ is now the first order diffraction angle after refraction into water. Note that $f = 1$ corresponds to the ideal case of 90° deflection toward one side, which would imply that 100% of the normally incident radiation pressure force is transferred to a unidirectional lateral reaction force.

2.2 | Training Set Structure

We implemented a tandem neural network using the Keras API within the TensorFlow framework to perform inverse design of the metavehicle metagrating (Figure 1A, B, Figure S1B). The training dataset comprised 30 000 samples, generated within broad geometrical parameter ranges of periodicity (P = 810–958 nm), height (H = 250–550 nm), ridge widths (W_1–W_3 = 40–400 nm), and gap (g = 40–150 nm). To ensure physically realizable structures, only combinations satisfying $W_1 < W_2 < W_3$ and $\xi = P - W_1 - W_2 - W_3 - 2g$ = 40–758 nm were considered. These conditions maintain sufficient ridge separation (≥40 nm) while maximizing the lateral force–related fitness function (Equation 2). A wide and well-spaced parameter grid was chosen to enhance the coverage of the geometrical design space, thereby improving the extrapolation capability of the network. Full implementation details, including hyperparameter optimization and training procedures, are provided in the Methods and Supplementary Information. Having defined the training set and physical constraints, we next employed a tandem neural network to perform the inverse design.

2.3 | Inverse Design by a Tandem Network

To achieve efficient inverse design of high-performance metavehicle metagratings, we employed a tandem fully connected neural network (Figure 1B, see Methods, Notes S1–S5, and Figures S1–S6). The tandem framework, previously demonstrated for metasurface design [30–35], consists of a forward prediction network that models the optical response from geometrical parameters and an inverse design network that predicts geometry from a desired optical response. During training, the outputs of the inverse network are connected to the inputs of the forward network with fixed weights, effectively constraining

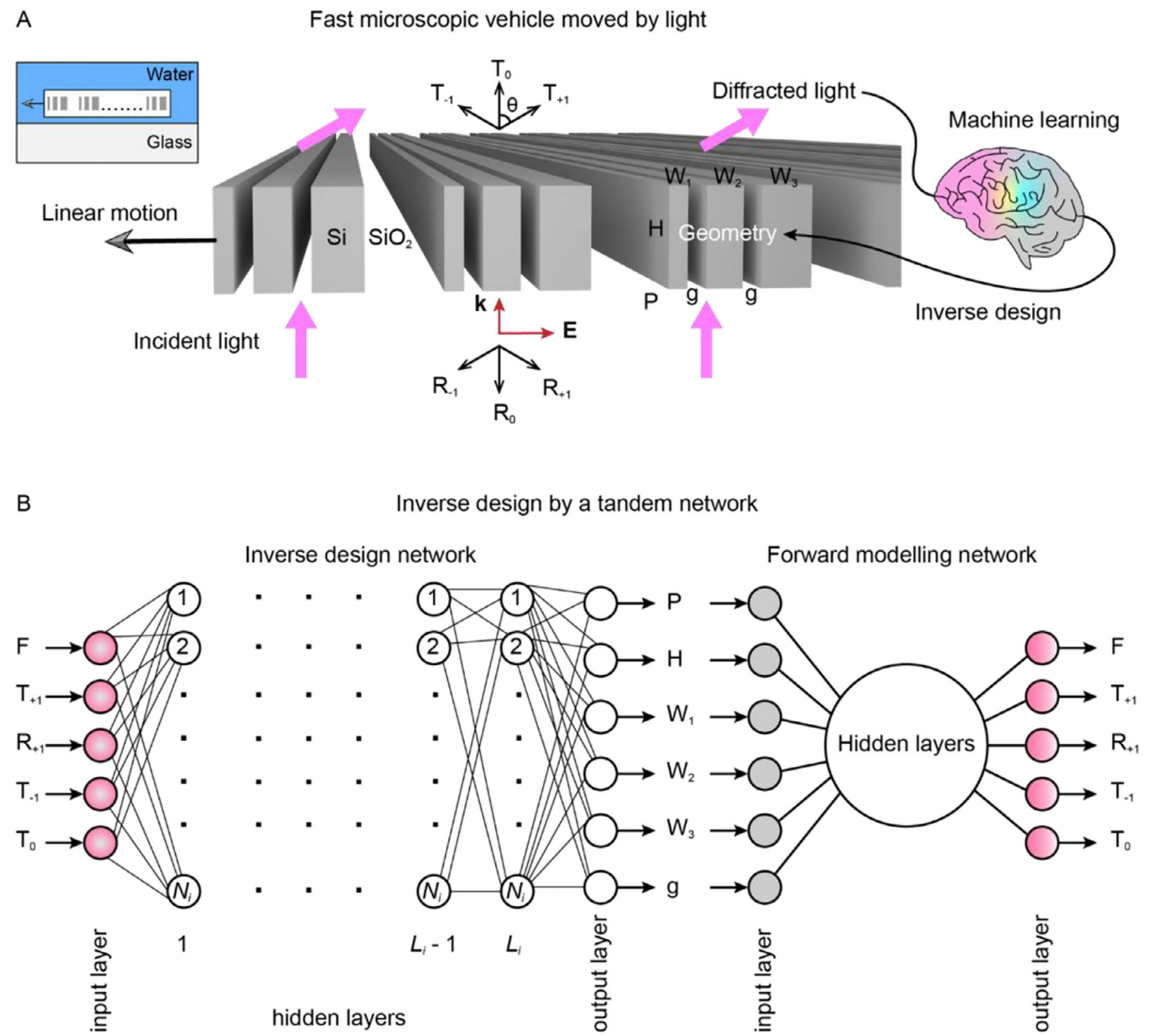

FIGURE 1 | (A) Schematic illustration of the optically propelled metavehicle. Left inset: experimental geometry showing propulsion across a glass substrate in water. Right inset: machine-learning-based inverse design workflow. (B) Architecture of the tandem neural network used for metagrating inverse design, consisting of forward and inverse subnets.

the system to physically realizable solutions and mitigating the non-uniqueness problem typical of inverse design [35].

The forward network (Figure S2) was trained first to predict diffraction efficiencies and fitness values from the 30 000 simulated samples, with 3000 additional samples used for validation. Hyperparameters, such as layer depth, neuron count, batch size, and learning rate, were optimized through five-fold cross-validation and random search. Early stopping and SELU activation were applied to ensure stable convergence (Figure S4) and normalized data flow.

The trained forward model achieved a mean absolute prediction error of $\Delta f \approx 1.2\%$, with more than 95% of validation samples predicted within 5% error and nearly 70% within 1%. The inverse network (Figure S3) was then trained by fixing all parameters of the forward model and updating only the inverse-model weights and biases. The resulting tandem network achieved a validation mean-squared error of $\approx 4.3 \times 10^{-3}$. These results demonstrate that the tandem framework provides a reliable and computationally efficient route to inverse design of metasurfaces with experimentally achievable geometries.

2.4 | Machine Learning Predictions and COMSOL Validation

The optimal geometrical parameters predicted using the trained tandem network were: $P = 847$ nm, $H = 393$ nm, $W_1 = 70$ nm, $W_2 = 140$ nm, $W_3 = 197$ nm, $g = 71$ nm. COMSOL simulations of this geometry confirmed the predicted optical response with excellent agreement, yielding a fitness value $f_{\mathrm{COMSOL}} = 87.8\%$,

TABLE 1 | Comparison of diffraction efficiencies and fitness f for the ML-optimized metagrating geometry. COMSOL simulations closely match network predictions, with errors below 1%, demonstrating the reliability of the tandem neural network for accurate inverse design. Tandem input: Target optical response values provided to the inverse network; Tandem output: Optical response predicted by the trained tandem network for the ML-optimized geometry; COMSOL: Full-wave simulation results for the ML-optimized geometry.

	f (%)	T_{+1} (%)	R_{+1} (%)	T_{-1} (%)	T_0 (%)
Tandem input	100	78	14	0.9	2.5
Tandem output	87.5	79	17	1.1	1.8
COMSOL	87.8	79.8	17	0.97	1.5

and diffraction efficiencies according to Table 1. Errors between network predictions and COMSOL outputs were below 1%, reflecting the high interpolation accuracy of the forward model within the well-defined parameter space.

To guarantee experimental feasibility, only designs satisfying $g \geq$ 70 nm and $W_1 \geq 60$ nm were considered (Table S1). Within this subset, the highest training-set fitness was 81.7%. Thus, machine learning increased achievable efficiency by 6% relative to the fabricable training set (Figure 3A), demonstrating that the model has learned to extrapolate beyond the training set. While some training samples exhibit higher fitness (up to 85.1%, Table S1), these corresponded to unrealistically small gaps ($g = 40$ nm) that we cannot fabricate in extended structures.

The inverse design network generates multiple high-performance geometries: 4281 fabricable samples with predicted $f \geq 85\%$ were identified, clustered near the optimal configuration (Figure 2). COMSOL parameter sweeps around the optimum indicate that the fitness peaks sharply at the predicted geometry, with deviations of ∼5 nm leading to <0.2% change in f (Figure S5).

Near-field simulations of the optimal geometry (Figure 3B) demonstrate strong one-sided diffraction into the +1 orders (T_{+1} = 79.8%, R_{+1} = 17%) with diffraction into remaining orders summing up to ≈ 3% only, consistent with requirements for efficient lateral optical propulsion. These results demonstrate that the tandem network accurately predicts geometries that are both highly efficient and experimentally realizable.

2.5 | Experimental Validation

Metavehicles with structure parameters close to the optimized design were fabricated in amorphous Si (a-Si) using a top-down process [15]. After release from the supporting substrate into water, a droplet of the solution was placed in a thin sample cell on an inverted microscope. Lateral propulsion experiments were conducted using a 1064 nm Gaussian laser beam, with controlled polarization and wide focus, entering from above. Metavehicle motion was quantified via video tracking, see Video S1 for an example, yielding lateral speed and orientation under different laser intensities and polarizations, as summarized in Figure 4.

The lateral speed v of a metavehicle is determined by the balance between the applied optical force and the friction force, which yields that $v \propto I_0 A f / \gamma$. Here, I_0 is the light intensity, A is the area of the metasurface, f is the conversion efficiency between incident radiation pressure force and lateral force (Equation 2), and γ is the friction constant for translation. In Figure 4B, we compare the measured maximum velocity of fabricated metavehicles to prior art [11]. The latter were based on metagratings composed of directional Si nanoantennas (Figure 4B) and had similar dimensions as the ones fabricated here (20 × 20 × 1 μm^3 vs. 21 × 19 × 1 μm^3 in [11]). As can be seen, we observe a speed enhancement of approximately a factor three compared to the results reported on in ref. [11]. This improvement can only be partly explained by an increase in calculated fitness, which corresponds to an enhancement of ∼1.6 ($f \approx 87\%$ compared to $f \approx 55\%$ in [11]). It is likely that the remaining difference mostly stems from differences in friction between the two samples, which could be due to several factors, such as the amount and absorptivity of the a-Si forming the metagratings, affecting the degree of photo-thermal heating and thereby the medium viscosity; surface charging and screening effects, affecting the distance between a metavehicle and the supporting substrate, and thereby the effective friction constant; and differences in surface roughness [11]. Nevertheless, it is obvious that the ML optimized metavehicles studied here exhibit substantially improved performance compared to prior art.

While the higher deflection angle compared to the original design reduces linear-polarization steerability, which is proportional to $\cos^2\theta_w$ [14], the vehicles remain controllable using circular polarization (Figure S8, Video S2). Furthermore, the propulsion speed varies with the angle φ between the incident linear polarization and the metasurface plane of diffraction: maximum speeds are achieved when the polarization is orthogonal to the ridges, as expected from our design criterion, while polarization parallel to the ridges results in minimal movement (Figure 4C, D). These results confirm that the ML-optimized metagrating both maximizes propulsion and exhibits predictable polarization-dependent behavior.

3 | Conclusion

We have demonstrated that machine-learning-based inverse design can effectively optimize lateral optical forces in microscopic metavehicles. By employing a tandem neural network, we efficiently explored a high-dimensional geometrical parameter space and identified metagrating designs that maximize the fitness function while remaining fabricable. COMSOL simulations confirmed the network predictions with <1% error, illustrating the accuracy and reliability of the approach.

Fabricated metavehicles based on an ML-optimized design exhibited substantially higher lateral propulsion speeds in water compared to a previously reported design, validating both the computational model and the practical feasibility of the predicted geometries. The experimental results also confirmed predictable polarization-dependent motion, highlighting the interplay between optical design and controlled micromanipulation.

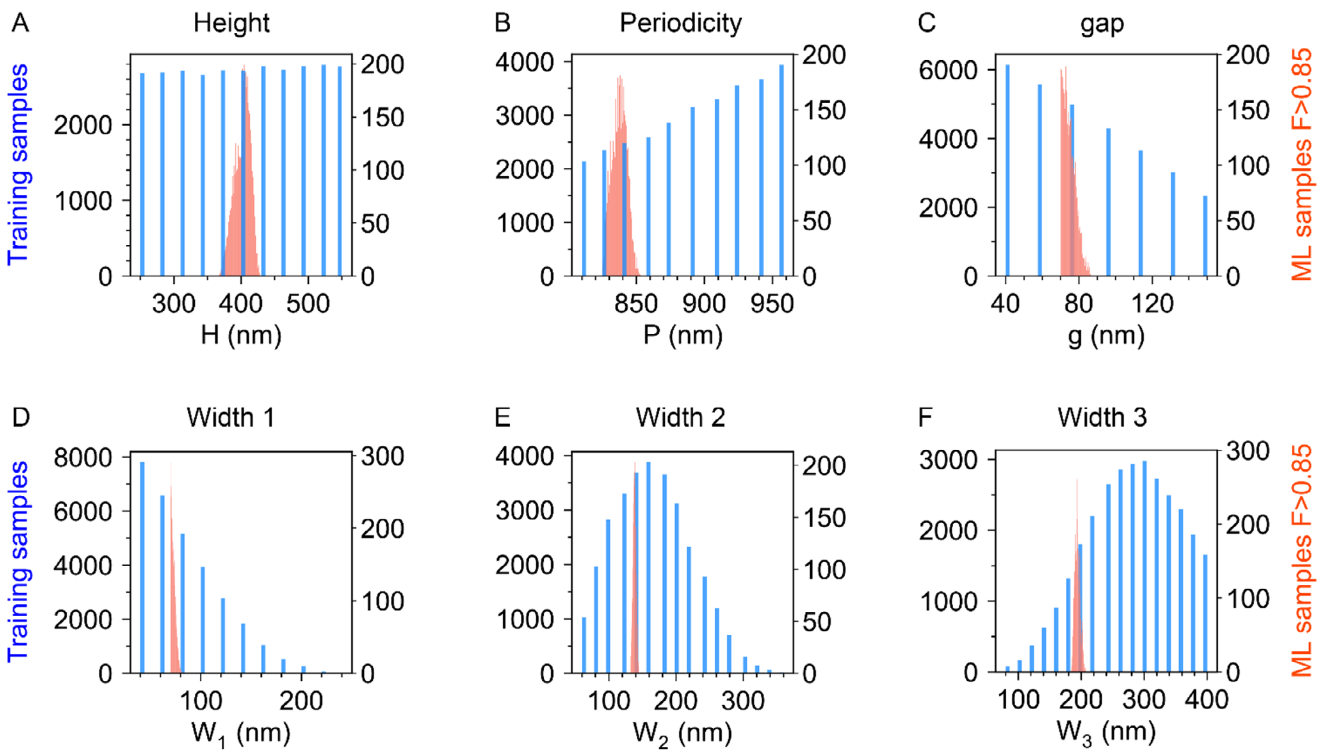

FIGURE 2 | Training-set composition and machine-learning output distribution. The training set contains 30 000 simulated samples (blue). The number of highly efficient geometries predicted by the inverse design network ($f > 0.85$) is shown in red (4281 samples). These cluster within a narrow region of the 6D geometrical parameter space. To ensure fabricability, the network is here restricted from producing designs with smallest feature size g, W_1 below 70 nm.

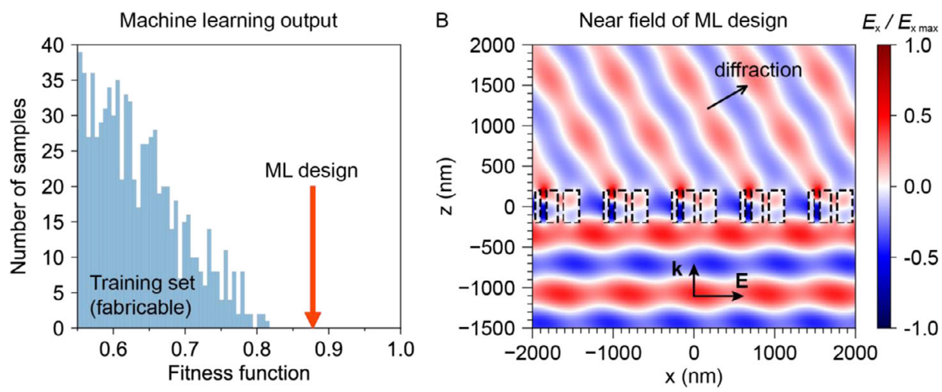

FIGURE 3 | Validation of the machine-learning-predicted metagrating design. (A) Fitness values (f) obtained by COMSOL for all samples, highlighting the ML-predicted optimal design (arrow) compared with the best fabricable (W_1 > 60 nm, g >70 nm) training-set structures (blue). (B) Near-field COMSOL simulation of the ML-optimized geometry showing strong one-sided diffraction into the +1 transmission order, consistent with highly efficient lateral optical force generation.

This work establishes a general and scalable framework for inverse design of optomechanical microdevices. Beyond metavehicles, the same methodology can be applied to a broad range of high-performance metasurfaces and photonic components, including beam deflectors, axicons, and metalenses. The combination of machine learning, physics-based simulations, and top-down fabrication provides a powerful route to accelerate discovery and optimize performance in nanoscale photonics, opening new possibilities for microfluidics, microbiology, and light-driven micromachines.

4 | Methods

4.1 | Electromagnetic Simulations

Diffraction efficiencies and near-field electric distributions were obtained using COMSOL Multiphysics. A 1D Si grating embedded in SiO_2 (n_{SiO2} = 1.45) was simulated with periodic boundary conditions in the lateral plane (Figure S1A). The incident plane wave was linearly polarized perpendicular to the grating ridges, generating p-polarized diffraction. The Si refractive index

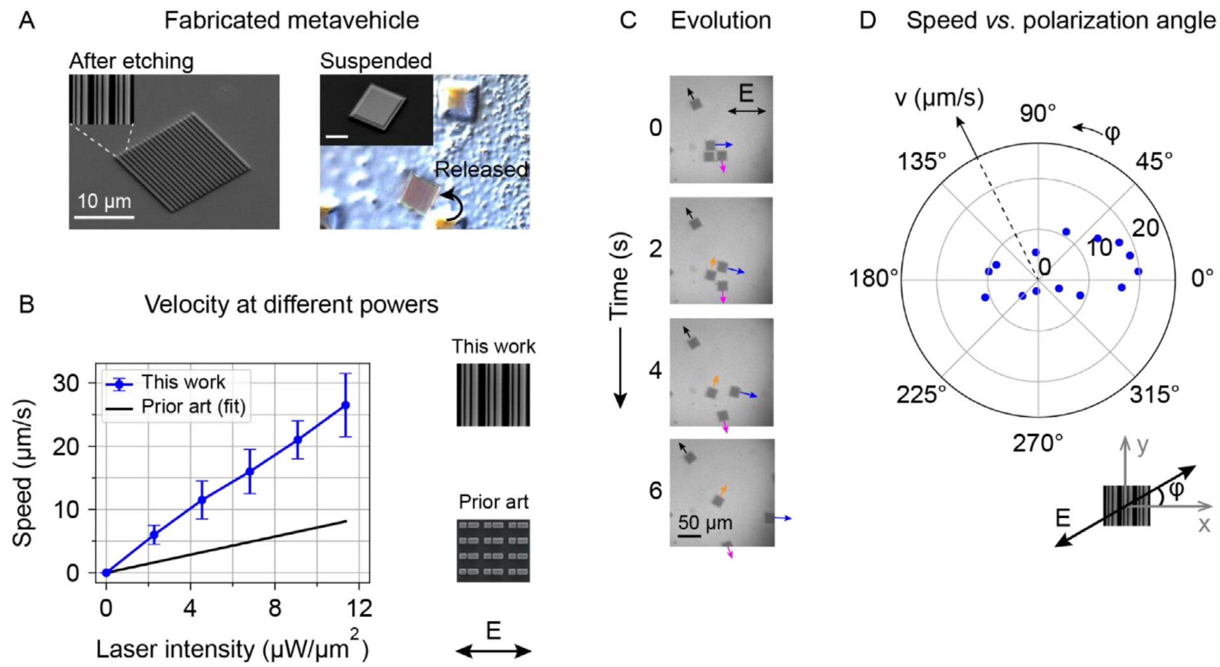

FIGURE 4 | A) SEM images of a fabricated metagrating after etching (left) and a metavehicle before and after it has been released from the substrate (right). Scale bars are 10 µm. (B) Measured maximum metavehicle speed vs incident laser intensity compared to Ref. [11]. The insets to the right show the two different metagrating designs and the error-bars indicate variations in maximum speed between different individual metavehicles and tracks. (C) Consecutive micrographs illustrating metavehicle propulsion in water. (D) Propulsion speed vs the angle φ between the metagrating plane of diffraction and the incident linear polarization ($\varphi = 0$ or 180° corresponds to polarization perpendicular to the grating lines). The structure parameters for the metavehicles were P = 856 nm ($\theta_w \approx 69°$), H = 393 nm, W_1 = 60 nm, W_2 = 143 nm, W_3 = 205 nm, and g = 70 nm.

was set to n_{Si} = 3.8 and we neglect absorption. Previously published results show that experimental diffraction data on macroscopic metagratings similar to the ones discussed here yield diffraction efficiencies in excellent agreement with COMSOL predictions [11, 14].

4.2 | Machine-Learning-Based Inverse Design

The inverse design of metavehicle metagratings was carried out using a tandem fully connected neural network implemented in Keras/TensorFlow, Python. The tandem architecture comprises a forward neural network, which predicts optical responses from geometrical parameters, and an inverse neural network, which predicts geometrical parameters from a desired optical response. The tandem framework allows for efficient exploration of the design space while mitigating the non-uniqueness problem common in inverse design.

4.3 | Training Datasets and Procedures

Training datasets and procedures are described in detail in (Notes S1–S5). Briefly, 30 000 geometries were randomly sampled from a well-defined 6D parameter space (P, H, W_1–W_3, g) for training, with an additional 3000 samples for validation. Fabrication constraints ($g \geq 70$ nm, $W_1 \geq 60$ nm) were enforced when generating high-efficiency candidates. All inputs were normalized, and SELU activations were used to maintain normalized flow through the network. The models were trained using the mean squared error (MSE) loss function with the Nadam optimizer. We further implemented early-stopping to counteract overfitting. Hyperparameters, including network depth, neurons per layer, batch size, and learning rate, were optimized using five-fold cross-validation and manual fine-tuning. The trained forward network achieved a mean absolute error (MAE) of 1.17% for the fitness function on the validation set. The tandem network successfully predicted thousands of geometries with $f \geq 0.85$, including the optimal design verified via COMSOL simulations.

4.4 | Fabrication

Metavehicles were fabricated using a top-down lithography approach based on ref. [15]. A 4-inch Si wafer was thermally grown with 400 nm SiO_2 and coated with 380 nm amorphous Si. Electron-beam lithography defined the metagrating patterns in a resist mask, followed by development. A hard mask (3 nm Cr / 50 nm Ni) was deposited, and patterns were transferred to Si via reactive-ion etching. An additional SiO_2 layer was deposited, and lithography step defined the metavehicle perimeters. Excess material and the hard mask were removed, and the metavehicles was liberated through isotropic etching in water. SEM imaging confirmed that the fabricated geometry closely matched the intended design.

4.5 | Optical Experiments

Lateral propulsion experiments were conducted using a 1064 nm Gaussian laser beam with beam-waist radius of ∼200 µm. Polarization was controlled via a half-wave plate (HWP) or quarter-wave plate (QWP) for circular polarization. Laser light was focused onto a 4 μL sample chamber (two microscope slides, 120 μm spacer) from above using a lens (f = 100 mm), and the chamber was observed in reflection using white light and a 40X, NA = 0.9, objective in an inverted microscope. Metavehicle motion was quantified via video tracking, yielding lateral speed and orientation under different laser intensities and polarizations. These measurements enabled estimating the experimental fitness function, which compared favorably to prior art.

4.6 | Artificial Intelligence Generated Content

We used ChatGPT as a companion in language and text editing.

Acknowledgements

This work was supported by the Knut and Alice Wallenberg Foundation. Nanofabrication was performed at MyFab Chalmers. The authors thanks Styrbjörn Käll for constructive comments.

Conflicts of Interest

The authors declare no conflicts of interest.

Data and Code Availability

Data and Code Are Available at //doi.org/10.34740/Kaggle/Dsv/14607125

References

1. N. Yu and F. Capasso, "Flat Optics With Designer Metasurfaces," *Nature Materials* 13 (2014): 139–150, https://doi.org/10.1038/nmat3839.

2. D. A. Neshev, "Optical Metasurfaces: New Generation Building Blocks for Multi-functional Optics," *Light: Science & Applications* 7 (2018): 58, https://doi.org/10.1038/s41377-018-0058-1.

3. T. Gu, H. J. Kim, C. Rivero-Baleine, and J. Hu, "Reconfigurable Metasurfaces towards Commercial Success," *Nature Photonics* 17 (2023): 48–58, https://doi.org/10.1038/s41566-022-01099-4.

4. M. L. P. Brongersma, A. Ragip, and H. Altug, "The Second Optical Metasurface Revolution: Moving From Science to Technology," *Nature Reviews Electrical Engineering* 2 (2025): 125–143, https://doi.org/10.1038/s44287-024-00136-4.

5. A. M. Afridi, N. Meyer, and R. Quidant, "Controlling the Sign of Optical Forces Using Metaoptics," *Nature Communications* 17 (2026): 1163, https://doi.org/10.1038/s41467-025-67928-6.

6. O. Ilic and H. A. Atwater, "Self-stabilizing Photonic Levitation and Propulsion of Nanostructured Macroscopic Objects," *Nature Photonics* 13 (2019): 289–295, https://doi.org/10.1038/s41566-019-0373-y.

7. R. Gao, M. D. Kelzenberg, Y. Kim, O. Ilic, and H. A. Atwater, "Optical Characterization of Silicon Nitride Metagrating-Based Lightsails for Self-Stabilization," *ACS Photonics* 9 (2022): 1965–1972, https://doi.org/10.1021/acsphotonics.1c02022.

8. L. Michaeli, R. Gao, and M. D. Kelzenberg, "Direct Radiation Pressure Measurements for Lightsail Membranes," *Nature Photonics* 19 (2025): 369–377, https://doi.org/10.1038/s41566-024-01605-w.

9. G. A. Swartzlander, "Radiation Pressure on a Diffractive Sailcraft," *Journal of the Optical Society of America B* 34 (2017): C25–C30, https://doi.org/10.1364/JOSAB.34.000C25.

10. M. Taghavi, M. M. Salary, and H. Mosallaei, "Multifunctional Metasails for Self-stabilized Beam-riding and Optical Communication," *Nanoscale Advances* 4 (2022): 1727–1740, https://doi.org/10.1039/D1NA00747E.

11. D. Andrén, et al., "Microscopic Metavehicles Powered and Steered by Embedded Optical Metasurfaces," *Nature Nanotechnology* 16 (2021): 970–974.

12. P. Lalanne, S. Astilean, P. Chavel, E. Cambril, and H. Launois, "Design and Fabrication of Blazed Binary Diffractive Elements With Sampling Periods Smaller Than the Structural Cutoff," *Journal of the Optical Society of America A* 16 (1999): 1143–1146, https://doi.org/10.1364/JOSAA.16.001143.

13. T. Li, J. J. Kingsley-Smith, and Y. Hu, "Reversible Lateral Optical Force on Phase-gradient Metasurfaces for Full Control of Metavehicles," *Optics Letters* 48 (2023): 255–258, https://doi.org/10.1364/OL.478979.

14. E. Engay, M. Shanei, and V. Mylnikov, "Transverse Optical Gradient Force in Untethered Rotating Metaspinners," *Light: Science & Applications* 14 (2025): 38, https://doi.org/10.1038/s41377-024-01720-x.

15. M. Shanei, G. Wang, P. Johansson, G. Volpe, and M. Käll, "Harnessing Photon Recoil for Enhanced Torque on Light-Driven Metarotors," *Nano Letters* 25 (2025): 4832–4837, https://doi.org/10.1021/acs.nanolett.4c06410.

16. G. Wang, M. Rey, and A. Ciarlo, "Microscopic Geared Metamachines," *Nature Communications* 16 (2025): 7767, https://doi.org/10.1038/s41467-025-62869-6.

17. Y. Y. Tanaka, P. Albella, M. Rahmani, V. Giannini, S. A. Maier, and T. Shimura, "Plasmonic Linear Nanomotor Using Lateral Optical Forces," *Science Advances* 6 (2020): abc3726, https://doi.org/10.1126/sciadv.abc3726.

18. X. Wu, R. Ehehalt, G. Razinskas, T. Feichtner, J. Qin, and B. Hecht, "Light-driven Microdrones," *Nature Nanotechnology* 17 (2022): 477–484, https://doi.org/10.1038/s41565-022-01099-z.

19. M. M. R. Elsawy, S. Lanteri, R. Duvigneau, J. A. Fan, and Genevet, "Numerical Optimization Methods For Metasurfaces," *Laser & Photonics Reviews* 14 (2020): 1900445.

20. B. Born, S.-H. Lee, J.-H. Song, J. Y. Lee, W. Ko, and M. L. Brongersma, "Off-axis Metasurfaces for Folded Flat Optics," *Nature Communications* 14 (2023): 5602, https://doi.org/10.1038/s41467-023-41123-x.

21. T. Ye, D. Wu, and Q. Wu, "Realization of Inversely Designed Metagrating for Highly Efficient Large Angle Beam Deflection," *Optics Express* 30 (2022): 7566–7579, https://doi.org/10.1364/OE.454137.

22. X. Zu, B. Chen, N. Tang, W. E. I. Sha, J. Wang, and M. Qiu, "Versatile Optical Beam Routers Based On Inversely Designed Supercell Metagratings," *Photonics and Nanostructures—Fundamentals and Applications* 52 (2022): 101075.

23. D. Midtvedt, V. Mylnikov, A. Stilgoe, M. Käll, H. Rubinsztein-Dunlop, and G. Volpe, "Deep learning in light–matter interactions," *Nanophotonics* 11 (2022): 3189–3214, https://doi.org/10.1515/nanoph-2022-0197.

24. F. Callewaert, V. Velev, P. Kumar, A. V. Sahakian, and K. Aydin, "Inverse-Designed Broadband All-Dielectric Electromagnetic Metadevices," *Scientific Reports* 8 (2018): 1358.

25. D. Sell, J. Yang, S. Doshay, R. Yang, and J. A. L.-A. Fan, "Multifunctional Metagratings Based on Freeform Multimode Geometries," *Nano Letters* 17 (2017): 3752–3757.

26. S. Colburn and A. Majumdar, "Inverse Design and Flexible Parameterization of Meta-optics Using Algorithmic Differentiation," *Communications Physics* 4 (2021): 65, https://doi.org/10.1038/s42005-021-00568-6.

27. B. M. A. G. Jokisch, B. Falkenberg, P. T. Kristensen, M. Wubs, O. Sigmund, and R. E. Christiansen, "Omnidirectional Gradient Force Optical Trapping in Dielectric Nanocavities by Inverse Design," *ACS Photonics* 11 (2024): 5118–5127, https://doi.org/10.1021/acsphotonics.4c01060.

28. B. M. A. C. Jokisch and R. Ellebæk, "Engineering optical forces Through Maxwell stress tensor inverse design," *Journal of the Optical*

Society of America B 42 (2025): 731–741, https://doi.org/10.1364/JOSAB.546272.

29. W. Xu, L. Hu, and K. Shao, "Design of Arbitrary Energy Distribution Beam Splitters Base on Multilayer Metagratings by a Hybrid Evolutionary Particle Swarm Optimization," *Optics Express* 31 (2023): 41339–41350, https://doi.org/10.1364/OE.502125.

30. I. Malkiel, M. Mrejen, A. Nagler, U. Arieli, L. Wolf, and H. Suchowski, "Plasmonic Nanostructure Design and Characterization via Deep Learning," *Light: Science & Applications* 7 (2018): 60, https://doi.org/10.1038/s41377-018-0060-7.

31. Z. Huang, X. Liu, and J. Zang, "The Inverse Design of Structural Color Using Machine Learning," *Nanoscale* 11 (2019): 21748–21758, https://doi.org/10.1039/C9NR06127D.

32. L. Xu, M. Rahmani, and Y. Ma, "Enhanced Light–Matter Interactions In Dielectric Nanostructures Via Machine-Learning Approach," *Advanced Photonics* 2 (2020): 1, https://doi.org/10.1117/1.AP.2.2.026003.

33. M. V. Zhelyeznyakov, S. Brunton, and A. Majumdar, "Deep Learning to Accelerate Scatterer-to-field Mapping for Inverse Design of Dielectric Metasurfaces," *ACS Photonics* 8 (2021): 481–488.

34. Z. Zhen, C. Qian, and Y. Jia, "Realizing Transmitted Metasurface Cloak by a Tandem Neural Network," *Photonics Research* 9 (2021): B229–B235, https://doi.org/10.1364/PRJ.418445.

35. D. Liu, Y. Tan, E. Khoram, and Z. Yu, "Training Deep Neural Networks for the Inverse Design of Nanophotonic Structures," *ACS Photonics* 5 (2018): 1365–1369, https://doi.org/10.1021/acsphotonics.7b01377.

Supporting Information

Additional supporting information can be found online in the Supporting Information section.

Supporting File:1 adom71396-sup-0001-SuppMat.docx.

Supporting File:2 adom71396-sup-0002-VideoS1.mp4.

Supporting File:3 adom71396-sup-0003-VideoS2.mp4.